Chinese Chemical Letters 37 (2026) 111926

Contents lists available at ScienceDirect

Chinese Chemical Letters

journal homepage: www.elsevier.com/locate/cclet

# Efficient large-current conversion of $CO_2$ to $C_2H_5OH$ *via* a *CO-*$OCH_2$ coupling pathway on alkanethiol-modified $Cu_2O$ array electrode

Min Zhang[a,b,1], Weimin Wang[a,b,1], Jun Li[a,b], Xun Zhu[a,b], Qian Fu[a,b,*]

[a] Key Laboratory of Low-grade Energy Utilization Technologies and Systems, Chongqing University, Ministry of Education, Chongqing 400044, China
[b] Institute of Engineering Thermophysics, School of Energy and Power Engineering, Chongqing University, Chongqing 400044, China

ARTICLE INFO

*Article history:*
Received 11 September 2025
Revised 29 September 2025
Accepted 29 September 2025
Available online 30 September 2025

*Keywords:*
$CO_2$ reduction
$C_2H_5OH$
$Cu_2O$-OTT
Asymmetric sites
*CO–*$OCH_2$ coupling

ABSTRACT

Developing advanced electrocatalysts to convert $CO_2$ into liquid fuels such as $C_2H_5OH$ is critical for utilizing intermittent renewable energy. The formation of $C_2H_5OH$, however, is generally less favored compared with the other hydrocarbon products from Cu-based electrocatalysts. In this work, an alkanethiol-modified $Cu_2O$ nanowire array (OTT-$Cu_2O$) was constructed with asymmetric Cu sites consisting of paired Cu–O and Cu–S motifs to overcome previous limitations of $C_2H_5OH$ electrosynthesis *via* $CO_2$RR pathway. This catalyst achieves a high Faradaic efficiency of 45% for $CO_2$-to-$C_2H_5OH$ conversion at 300 mA/cm$^2$, representing a more than two-fold enhancement over the $Cu_2O$ electrode. Mechanistic investigations reveal that the Cu–S site exhibits distinct C-binding capability that stabilizes key intermediates (*$OCH_2$ and *CO), in contrast to the O-affinitive Cu–O site. The asymmetric S–Cu–O configuration promotes thermodynamically favorable asymmetric C–C coupling between *CO and *$OCH_2$, forming the critical CO–$OCH_2$ intermediate and facilitating $C_2H_5OH$ production, as opposed to symmetric O–Cu–O sites that mainly generate HCOOH. This work offers an effective strategy for designing multi-active-site catalysts toward highly selective $CO_2$ reduction to $C_2H_5OH$ and provides fundamental insight into the reaction mechanism.

© 2025 Published by Elsevier B.V. on behalf of Chinese Chemical Society and Institute of Materia Medica, Chinese Academy of Medical Sciences.

Zero-gap membrane electrode assembly electrolyzer significantly reduces the inter-electrode distance and markedly improve energy efficiency, which is conducive to promote industrial electrosynthesis [1–5]. The electrocatalytic reduction of $CO_2$ ($CO_2$RR) to valuable fuels and feedstocks using renewable electricity presents a carbon-neutral pathway for sustainable fuel generation [6]. Among various hydrocarbons and oxygenates, ethanol ($C_2H_5OH$) stands out as an important liquid product due to its widespread applications as an organic solvent, disinfectant, and fuel additive [7,8]. Thus, the efficient electrosynthesis of $C_2H_5OH$ from $CO_2$ holds considerable economic and environmental significance.

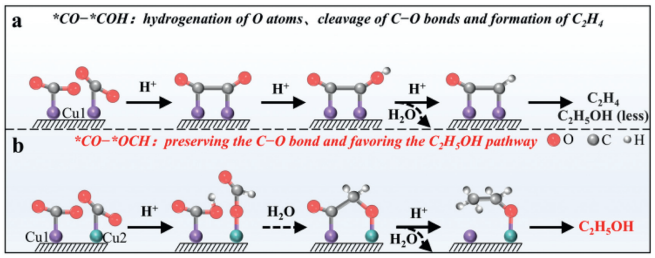
Recently, numerous copper-based catalytic sites, including homo-Cu sites and multi-Cu sites structures, have been designed to enhance the $CO_2$RR performance toward $C_2H_5OH$ [9–11]. However, in most cases, the Faradaic efficiency for $C_2H_5OH$ ($FE_{C_2H_5OH}$) remains lower than that for ethylene ($C_2H_4$), another major $C_2$ product. This discrepancy primarily stems from the higher energy barrier associated with $C_2H_5OH$ formation [12,13]. Specifically, during $CO_2$RR, both $C_2H_5OH$ and $C_2H_4$ share a common key intermediate, *CO–*COH (where * denotes an adsorption site) [14]. It is crucial to note that for $C_2H_5OH$ to be produced, one of the two C–O bonds in the *CO–*COH intermediate must be preserved [15].

However, during the $CO_2$RR process, the key intermediate *CO–*COH becomes coordinated to two Cu sites *via* each of its C atoms. This bidentate coordination facilitates the hydrogenation of O atoms, promoting facile cleavage of the C–O bond and leading preferentially to $C_2H_4$ formation (Scheme 1a) [16]. Moreover, the adsorbed *CO–*COH species may undergo structural rearrangement, transforming into an enol-like configuration where one of the C atoms originally bound to Cu is replaced by an O atom. Nevertheless, even in this enol-form intermediate, C–O bond rupture remains favorable, resulting again in $C_2H_4$ as the dominant product [17]. Consequently, the $FE_{C_2H_5OH}$ is typically two to three times lower than that for $FE_{C_2H4}$, highlighting the significant challenge in achieving high selectivity of $C_2H_5OH$ by Cu-based catalysts with homo-sites and multi-sites. Therefore, developing more efficient catalyst architectures and gaining deeper mechanistic insights into the pathways are essential for advancing $CO_2$RR toward practical $C_2H_5OH$ synthesis.

A promising strategy to suppress $C_2H_4$ formation and promote ethanol selectivity involves steering the $CO_2$RR pathway toward distinct mechanistic routes for $C_2H_5OH$ production [18,19].

* Corresponding author.
*E-mail address:* fuqian@cqu.edu.cn (Q. Fu).
[1] These authors contributed equally to this work.

https://doi.org/10.1016/j.cclet.2025.111926
1001-8417/© 2025 Published by Elsevier B.V. on behalf of Chinese Chemical Society and Institute of Materia Medica, Chinese Academy of Medical Sciences.




**Scheme 1.** Poroposed reaction paths for yielding $C_2H_4$ *vs.* $C_2H_5OH$ on the surface of (a) symmetric $Cu^1$-$Cu^1$ sites and (b) asymmetric $Cu^1$-$Cu^2$ sites in this work.

This alternative mechanism proceeds through unique $C_1$ and $C_2$ intermediates and involves an unconventional C–C coupling step. By enabling one of the $C_1$ intermediates to coordinate to the metal center *via* its O atom, rather than the C atom, premature hydrogenation of O can be circumvented, thereby preserving the C–O bond and favoring $C_2H_5OH$ formation [20]. Theoretical studies have identified several such O-bound intermediates, including *OC, *OCHO, *$OCH_2OH$, and *$OCH_2$ [21,22]. Furthermore, an asymmetric C–C coupling between *$OCH_2$ and another $C_1$ species, *CO, can generate the critical intermediate CO–$OCH_2$ (Scheme 1b), which exhibits a higher propensity toward $C_2H_5OH$ than $C_2H_4$ [23–25]. Consequently, it is imperative that adjacent copper atoms in the catalytic site possess asymmetric electronic or geometric properties to facilitate this distinct reaction pathway.

Cu-based catalysts with strong affinity for O atoms are conducive to the formation of *$OCH_2$ during $CO_2$RR process. In particular, cuprous oxide ($Cu_2O$) has been reported to preferentially stabilize *OCHO with respect to *CO species [26,27], which accounts for its widespread application in the electrosynthesis of HCOOH. Recent studies show that introducing $Cu^+$ vacancies into $Cu_2O$ *via* surface modification can selectively enhance the adsorption and fixation of *CO [28]. These findings indicate that adjacent active sites within copper catalysts, featuring distinct affinities for carbon and oxygen, respectively, can simultaneously promote the generation of *CO and *$OCH_2$ species. This asymmetric environment facilitates the critical C–C coupling between *CO and *$OCH_2$, forming the *CO–*$OCH_2$ intermediate and ultimately promoting the selective production of $C_2H_5OH$ from $CO_2$, enriching the local reaction concentration at the catalytic surface.

To verify the above hypothesis, the alkanethiols molecule-modified $Cu_2O$ nanowire array (OTT-$Cu_2O$) with unprecedented asymmetric Cu sites (namely, a pair of Cu–O and Cu–S sites) was designed to overcome aforementioned limitation, which exhibits an impressive selectivity of $CO_2$RR to $C_2H_5OH$ reaches up to 45 % at 300 mA/$cm^2$, representing a more than two-fold improvement compared to the $Cu_2O$ electrode. Mechanistic studies indicate that, in contrast to the Cu–O site which exhibits higher oxygen affinity, the Cu–S site facilitates unique carbon bonding, playing a critical role in stabilizing key intermediates such as *$OCH_2$ and *CO. Consequently, the asymmetric S–Cu–O sites are shown to be thermodynamically more favorable for the asymmetric C–C coupling between *CO and *$OCH_2$, leading to the formation of the critical CO–$OCH_2$ intermediate, compared to symmetric O–Cu–O sites that mainly produce HCOOH. This configuration significantly promotes the selective formation of $C_2H_5OH$. This work not only establishes a promising strategy for achieving high selectivity in $CO_2$-to-$C_2H_5OH$ conversion through the rational design of multi-active-site catalysts, but also provides deeper mechanistic insights into the pathway of $CO_2$ reduction toward $C_2H_5OH$.

Copper mesh (CM, 200 mesh) was purchased from anping hangying silkscreen Co., Ltd. Potassium bicarbonate ($KHCO_3$, >99.5 %), potassium hydroxide (KOH, >90 %), hydrochloric acid (HCl, 36 %–38 %) and anhydrous ethanol ($C_2H_5OH$, >99.7 %) were purchased from Chengdu Kelong Chemical Co., Ltd. Phosphoric acid ($H_3PO_4$, >85 %) was obtained from Chongqing Chuandong Chemical Co., Ltd. Dimethylsulfoxide (DMSO, 99.8 %), deuterium oxide ($D_2O$, 99.9 %), and 1-octadecanethiol ($C_{18}H_{38}S$, 97 %) was acquired from Aladdin Co., Ltd. All reagents were used as received without further purification. Deionized water (18.2 MΩ/cm) was generated from an ultra-pure purified water system.

Pretreatment of Cu mesh: The purchased Cu mesh cleaned in a variety of ways. Firstly, Cu mesh was washed with HCl to remove surface impurities. Whereafter, surface electropolish was conducted in a two-electrode system by using 85 % $H_3PO_4$ solution as electrolyte, Cu mesh as working electrode ($2 \times 2$ $cm^2$), and a platinum plate as counter electrode, respectively. A constant voltage of 4 V was applied to the Cu surface for 75 s. After polishing, the electrode was washed with deionized water several times.

Preparation of $Cu_2O$ nanowires ($Cu_2O$ electrode): The dense $Cu_2O$ nanoneedles layers can synthesize by electrochemical oxidation coupled with heating dehydration strategy. Firstly, the cleaned Cu mesh as anode electrode was immersed in 3 mol/L KOH electrolyte, a platinum plate as counter electrode, and Ag/AgCl as reference electrode, respectively. A constant current of 11 mA/$cm^2$ was applied for 350 s to obtain $Cu(OH)_2$ nanoneedles. Afterward, $Cu(OH)_2$ nanoneedles were dehydrated at 180 °C for 1 h, and the $Cu_2O$ electrode was prepared.

Preparation of OTT modified $Cu_2O$ nanowires ($Cu_2O$-OTT electrode): The hydrophilic $Cu_2O$ was immersed in an $N_2$-saturated ethanol solution containing 10 mmol/L of 1-octadecanethiol at 60 °C in continuous $N_2$ flow for natural drying, and the $Cu_2O$@OTT electrode was prepared. Subsequently, the $Cu_2O$@OTT precursor was electrochemically converted to OTT-$Cu_2O$ by applying a potential of −1.4 V *vs.* Ag/AgCl for 30 min in a $CO_2$-saturated 0.5 mol/L $KHCO_3$ electrolyte.

X-ray diffraction (XRD) measurements were performed on D8 ADVANCE X-ray diffractometer from Bruker AG at 40 kV and 40 mA using Cu K$\alpha$ radiation. X-ray photoemission spectroscopy (XPS) data were collected on a ESCALAB250Xi spectrometer equipped with an Al-K$\alpha$ radiation source (1486.6 eV) using C 1s (284.8 eV) as the reference. Fourier transform infrared spectroscopy (FTIR) measurements were recorded on Nicolet IS 10. Scanning electron microscopy (SEM) images were acquired on GeminiSEM 300 with an accelerating voltage of 3 kV. Transmission electron microscope (TEM) images and EDX mapping images were taken on JEM1200EX with an operated voltage at 200 kV. X-ray absorption fine structure (XAFS) measurement was collected on an Easy XAFS300+ system, and the acquired data were processed *via* the standard procedure using the ATHENA module of Demeter software packages. The contact angle was measured using a contact angle measuring instrument XC-CAM. The gas-phase product was detected by gas chromatography (GC) from Agilent 8890. The liquid phase product was tested by nuclear magnetic resonance (NMR) from Bruker AVANCE III. 600 M. *In-situ* ATR-SEIRAS spectra were collected by an FT-IR spectrometer (IRTracer100+CHI 660E) equipped with an MCT-A detector at different applied potentials. *In-situ* Raman spectra obtained by the LabRAM HR Evolution at different applied potentials.

Electrochemical characterization of the prepared electrodes was performed on an electrochemical workstation (VMP3, Biologic) in a two-electrode MEA system (Wuhan Zhisheng New Energy Co., Ltd.), which is comprised of the $Cu_2O$@OTT electrode cathode, an nickel foam anode, and a piece of Nafion 115 membrane. During electrolysis, the $CO_2$-saturated 1 mol/L $KHCO_3$ was directly fed to cathodic compartment at a rate of 100 mL/min, and 1 mol/L KOH was forced to continuously circulate through the anode compartment with a rate of 40 mL/min. Chronopotentiometry measurements were performed in the current density of 50 mA/$cm^2$ to

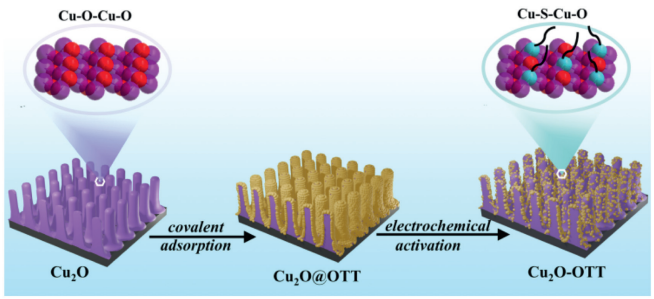



**Fig. 1.** Schematic illustration of the synthesis of asymmetric Cu–S–Cu–O sites.

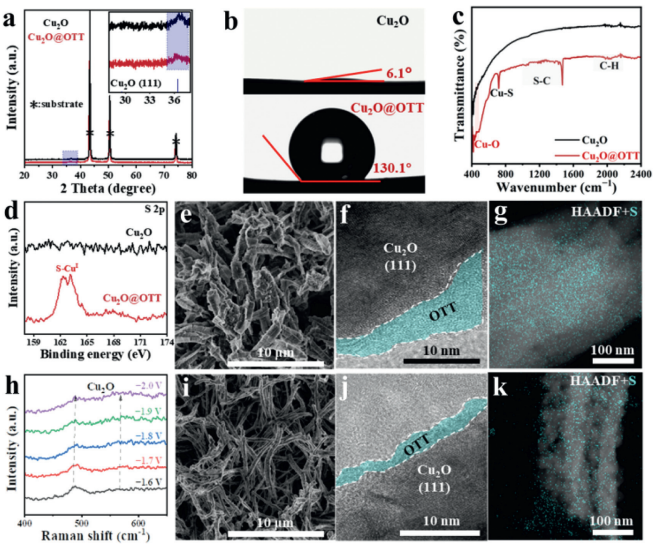



**Fig. 2.** Composition and structure characterizations: (a) XRD pattern, (b) the contact angle, (c) FTIR spectra, (d) S 2p XPS spectra of $Cu_2O$ and $Cu_2O$@OTT. (e) SEM image, (f) TEM image, (g) HAADF-STEM image of $Cu_2O$@OTT. (h) *In-situ* Raman spectra of $Cu_2O$@OTT at electrolysis from −1.6 V to −2.0 V *vs.* Ag/AgCl in $CO_2$-saturated 0.5 mol/L $KHCO_3$. (i) SEM image, (j) TEM image, (k) HAADF-STEM image of $Cu_2O$-OTT. Equivalent images from i-to-k after electrolysis at −1.4 V *vs.* Ag/AgCl in $CO_2$-saturated 0.5 mol/L $KHCO_3$ for 30 min.

600 mA/cm$^2$, and full-cell voltages reported were non-iR corrected full-cell potentials.

In general, the thiol end group are among the most stable, suggesting that, even under electrochemical reducing conditions, the ligand could remain chemisorbed to the catalyst surface. To address the simultaneous the requirements, we engineered a hierarchical $Cu_2O$ nanowires array with a thiol-modified surface (Fig. 1). Initially, copper hydroxide ($Cu(OH)_2$) nanowires on Cu foam ($Cu(OH)_2$ NWs) were prepared *via* a straightforward oxidizing process. After annealing under argon condition, these were transformed into $Cu_2O$ NWs, subsequently converted into OTT-$Cu_2O$ NWs array by simple wet-chemical adsorption combined with electrochemical activation strategies. As shown in Fig. S1 (Supporting information), for $Cu_2O$ NWs, SEM images feature its one-dimensional wire with a smooth surface, and the fine wire average diameter *circa* of 100 nm. Afterward, the resulting $Cu_2O$ NWs were immersed in an $C_2H_5OH$ solution containing 1-octadecanethiol (OTT) for the synthesis of $Cu_2O$@OTT, and then subjected to an electrochemical activation to remove excess weak molecular layer, leading to a strongly bonded OTT molecular surface on the one-dimensional wire ($Cu_2O$-OTT), which feature asymmetric Cu–S–Cu–O sites for significantly enhancing $CO_2$-to-$C_2H_5OH$ conversion.

The powder X-ray diffraction (XRD) pattern of as-prepared $Cu_2O$ electrode exhibited a characteristic peak corresponding to the (111) plane of $Cu_2O$ (Fig. 2a), which is more favorable to bond *OCHO species. After OTT modification, no additional diffraction peaks emerged in the XRD pattern, indicating that the crystalline structure of $Cu_2O$ remained unaltered. To confirm the existence of the OTT layer, contact angle measurements were conducted and results shown in Fig. 2b, the electrode contact angle to increase dramatically from 6.1° to 130.1° after OTT modification. Moreover, the strong Fourier transform infrared spectroscopy (FTIR) absorption bands at 785, 1473 and 2067 cm$^{-1}$ (Fig. 2c) further suggested that OTT covered the surface of $Cu_2O$ electrode. The successful functionalization with the OTT was further corroborated through X-ray photoelectron spectroscopy (XPS) spectroscopy. As shown in Fig. S3 (Supporting information), C, S, O, and Cu elements in $Cu_2O$@OTT electrode. Prior to treatment, $Cu_2O$ exhibited characteristic peaks consistent with $Cu_2O$ at 932.5 and 952.4 eV, while corresponding to $Cu^{2+}$ environments at 942.7 and 962.9 eV. After thiolation of the OTT layer, the $Cu^{2+}$ environment on the surface was removed, leaving Cu-S bonds and forming a $Cu^{+}$ surface (Fig. S4 in Supporting information). Additionally, a new S 2p peak appeared at 163.0 eV, indicating the presence of Cu-S bonds (Fig. 2d).

SEM of the $Cu_2O$ NWs after treatment confirmed that the nanostructure remained intact (Fig. 2e and Fig. S2 in Supporting information) and was coated with a monolayer between 4 nm and 5 nm in thickness (Fig. 2f). Through HAADF-STEM element-specific signal analysis, S elemental mapping analysis visually demonstrates uniform coverage of OTT on the $Cu_2O$ surface (Fig. 2g). After maintaining a reduction potential in $CO_2$-saturated 0.5 mol/L $KHCO_3$ electrolyte for over 30 min, the activation of the $Cu_2O$@OTT electrode was converted into a $Cu_2O$-OTT electrode. Meanwhile, the presence of $Cu_2O$ species are confirmed by *in-situ* Raman spectra during electrolysis (Fig. 2h and Fig. S6 in Supporting information). SEM characterization confirmed that the activated $Cu_2O$-OTT electrode retained its integrity (Fig. 2i and Fig. S5 in Supporting information), the $Cu_2O$ (111) crystal plane still presented, and the $Cu_2O$ surface still retains an approximately 2 nm-thick OTT layer (Fig. 2j), consisting with a surface of 1-octadecanethiol molecules bound upright (the chain length is 2.3 nm between the surface-bound S and terminal C). HAADF-STEM elemental analysis revealed that although the OTT coverage decreased after electrochemical activation, it maintained uniform distribution (Fig. 2k), which indicates selective peeling of partial OTT layers during potential application. Preliminary electrochemical characterization demonstrates that the ECSA decreases after OTT coating, the active area of $Cu_2O$-OTT electrodes (1.98 mF/cm$^2$) is smaller than that of $Cu_2O$ electrodes (6.26 mF/cm$^2$) (Fig. S7c in Supporting information), which stems from reduced electrolyte contact area due to hydrophobic surface properties.

X-ray absorption spectroscopy (XAS) was employed to characterize the chemical states and local fine structures of the Cu in $Cu_2O$ before and after OTT modification. The X-ray absorption near-edge structure (XANES) spectra in Fig. 3a reveal that the absorption edge positions of $Cu_2O$-OTT shifting to the higher energy side with respect to $Cu_2O$, which indicates that $Cu_2O$-OTT had a different coordination environment from that of $Cu_2O$. As shown in Fig. 3b, the valence of $Cu_2O$ lies between the characteristic values of $Cu_2O$ *Re* and Cu *Re*, whereas the $Cu_2O$-OTT is sized of a valence between $Cu_2O$ *Re* and standard CuO *Re*, implying that the oxidation state of Cu in $Cu_2O$ increase after the modification of OTT coating layers. The Fourier transform extended k-edge X-ray absorption fine structure (EXAFS) spectra in Fig. 3c reveals that $Cu_2O$-OTT consisted of Cu–O, Cu–S, and Cu–Cu bonds with simulated coordination numbers of 1.13, 1.85, and 2.43 Å, respectively. While the fitting results of $Cu_2O$ show that coordination numbers of Cu-O and Cu-Cu bonds are 1.75 and 2.61 Å, suggesting the formation of many unsaturated sites in $Cu_2O$ after OTT modification. Wavelet transform extended XAFS (WT-EXAFS) spectra was conducted to further highlight the local structural changes in $Cu_2O$ (Fig. 3d). The

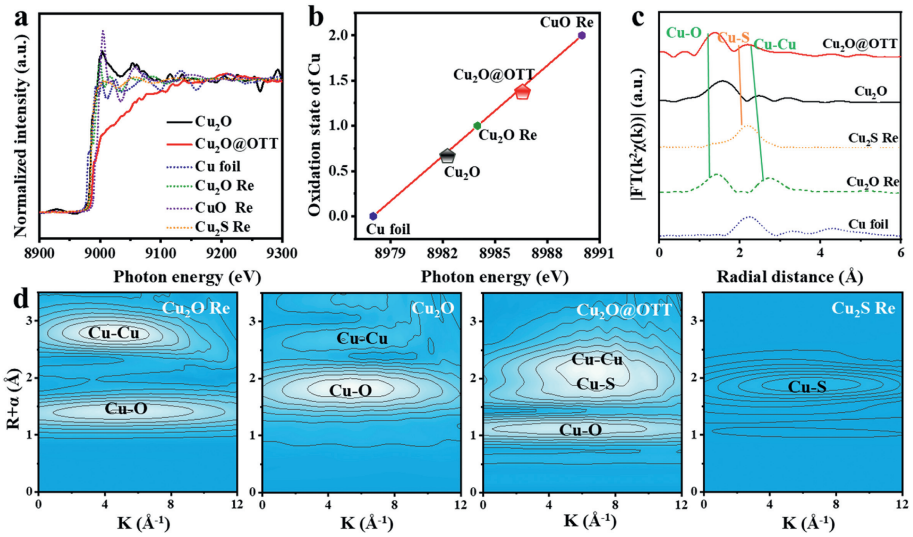



**Fig. 3.** XAS characterizations: (a) Normalized Cu K-edge XANES spectra of $Cu_2O$ and $Cu_2O$@OTT with the references. (b) the mean chemical valence analysis of Cu species. (c) FT-EXAFS spectra of $Cu_2O$ and $Cu_2O$@OTT with the references. (d) wavelet transform for the Cu K-edge EXAFS spectra of $Cu_2O$ Re, $Cu_2O$, $Cu_2O$@OTT and $Cu_2S$ Re.

reduced backscattering amplitude at Cu–O in $Cu_2O$-OTT compared with $Cu_2O$, indicating the lower coordination state of $Cu_2O$-OTT. As a result of OTT modification, unprecedented asymmetric Cu sites (namely, a pair of Cu–O and Cu–S sites) was successfully created for the further selective reduction of $CO_2$.

To evaluate the $CO_2$RR activity of the OTT-modified $Cu_2O$ electrode, the electrocatalytic $CO_2$RR performance was measured in a zero-distance electrolyzer with a $CO_2$-saturated 0.5 mol/L $KHCO_3$ electrolyte at applied current density from 50 mA/cm$^2$ to 500 mA/cm$^2$ (Figs. S8 and S9 in Supporting information). The products were characterized by nuclear magnetic resonance (NMR) and gas chromatography (GC), including CO, HCOO-, $CH_4$, and $C_{2+}$ products ($C_2H_4$, $C_2H_5OH$, $CH_3COOH$ and $C_3H_7OH$) (Fig. S10 in Supporting information). Fig. 4a shows the LSV of the hydrophobic $Cu_2O$@OTT electrode and equivalent wettable $Cu_2O$ electrode in a $CO_2$-saturated $KHCO_3$ electrolyte (0.5 mol/L, pH 6.8). To achieve a current density of −300 mA/cm$^2$, the $Cu_2O$ electrode required a voltage of 2.78 V, whereas the $Cu_2O$-OTT electrode required a significantly higher voltage of 3.15 V. This reduction in current density at a given voltage is partially attributable to the lower ECSA of the hydrophobic electrode.

The distribution of gases and liquid products generated are presented in Figs. 4b and c. For $Cu_2O$ electrode, $HCOO^-$ is the primary product along with little $C_2H_5OH$. As the current density becomes large, $C_2H_4$ and $CH_4$ products begin to appear, while the maximum $FE_{C2H5OH}$ reached only 18% at 100 mA/cm$^2$ (Fig. 4b). However, $C_2H_5OH$ is the primary product for $Cu_2O$-OTT electrode, reaching a peak Faradaic efficiency of 45% at 300 mA/cm$^2$ (Fig. 4c). It is worth noting that the selectivity of $H_2$ over $Cu_2O$ electrode does not change significantly after OTT modification. To visually represent the influence of OTT on the reduction products, the selectivity data is re-plotted in Fig. 4d. The $FE_{C2+}$ of the CuO-OTT electrode is 60%, contrasting with 30% for the $Cu_2O$ electrode, with $C_2H_5OH$ comprising the majority of $C_{2+}$ products, showcasing an enhancement of more than 2-fold. Besides, the ratio of $C_{2+}/HCOO^-$ is 4.8 for CuO-OTT at 600 mA/cm$^2$, which is much higher than that of $Cu_2O$ (Fig. 4e). Furthermore, energy efficiency of $C_2H_5OH$ for $Cu_2O$-OTT is also significantly higher with respect to $Cu_2O$ (Fig. S11 in Supporting information). Notably, to the best of our knowledge, the outstanding $CO_2$RR performance of $Cu_2O$-OTT for $C_2H_5OH$ production is record high in comparison with the previously reported (Fig. 4f and Table S1 in Supporting information).

As shown in Fig. 4g, the $Cu_2O$-OTT electrode exhibited a relatively stable bias under a constant current density of 200 mA/cm$^2$, with a negligible performance degradation within 10 h, evidencing the excellent stability of $Cu_2O$-OTT electrode under $CO_2$RR operating conditions. In addition, SEM image illustrates that the nanowire structure is maintained, XRD analysis confirmed retention of the $Cu_2O$ (111) crystal plane in the $Cu_2O$-OTT electrode, while XPS detected persistent S species. Contact angle measurements further demonstrated maintained hydrophobicity, collectively illustrating excellent stability and activity (Fig. S12 in Supporting information).

Typical Cu-based electrocatalysts cannot achieve high $FE_{C2H5OH}$ due to the competitive thermodynamics of the products of $C_2H_4$. To further investigate the possible reaction pathways and intermediates of the $CO_2$RR to $C_2H_5OH$ on the $Cu_2O$-OTT surface, *in situ* spectroscopy are performed in $CO_2$-saturated 0.5 mol/L $KHCO_3$ electrolyte (Fig. 5a, Figs. S13 and S14 in Supporting information). In our observations, we noted five distinct infrared signals at 1120, 1226, 1473, 1583, and 1646 cm$^{-1}$ for $Cu_2O$-OTT during continuous operation (Fig. 5b). The first peak signal at 1120 cm$^{-1}$ corresponds to the key intermediate $*OC_2H_5$ involved in the conversion of $CO_2$ to $C_2H_5OH$ [29]. The simultaneous observation of C–C (1226 cm$^{-1}$) and C–O (1253 cm$^{-1}$) vibrational peak signals further verified the formation of the $C_2H_5OH$ [30]. It is worth noting that the characteristic peak signal at 1583 cm$^{-1}$ can be attributed to the $C_2H_5OH$ key coupling $*CO–*OCH_2$ intermediate over the asymmetric S-Cu-O sites, which is generated by C–C coupling through *OCH and *CO [31]. By contrast, the main characteristic peak signals of the $Cu_2O$ appear at the *OCHO intermediate displayed at 1450 cm$^{-1}$ and the $*H_2O$ around 1650 cm$^{-1}$ (Fig. 5c).

In Raman spectra (Fig. 5d), two regions appearing at about 283 and 374 cm$^{-1}$ for $Cu_2O$-OTT are associated with the surface-absorbed *CO, belonging to the Cu–CO frustrated rotation and Cu–CO stretch, respectively [10,13,15]. At the same time, two extra bands appearing at 1435 and 1580 cm$^{-1}$ for the $Cu_2O$-OTT were also noticed at all testing potentials. The former is tentatively assigned to the symmetric stretching vibration of the carboxylate group (namely, *ν*–O–(CH)–O), corresponding to the surface-adsorbed *OCHO intermediates [32]. While the band at 1580 cm$^{-1}$ is assigned to the C=O stretching mode of surface-adsorbed $*CH_xCO$ species [33], a pivotal intermediate responsible for the yielding of $C_2H_5OH$, which maybe originate from the asymmetric C–C coupling between the *CO and *OCHO species on $Cu_2O$-OTT with Cu–O and Cu–S pairs. In comparison, only a peak at 1435

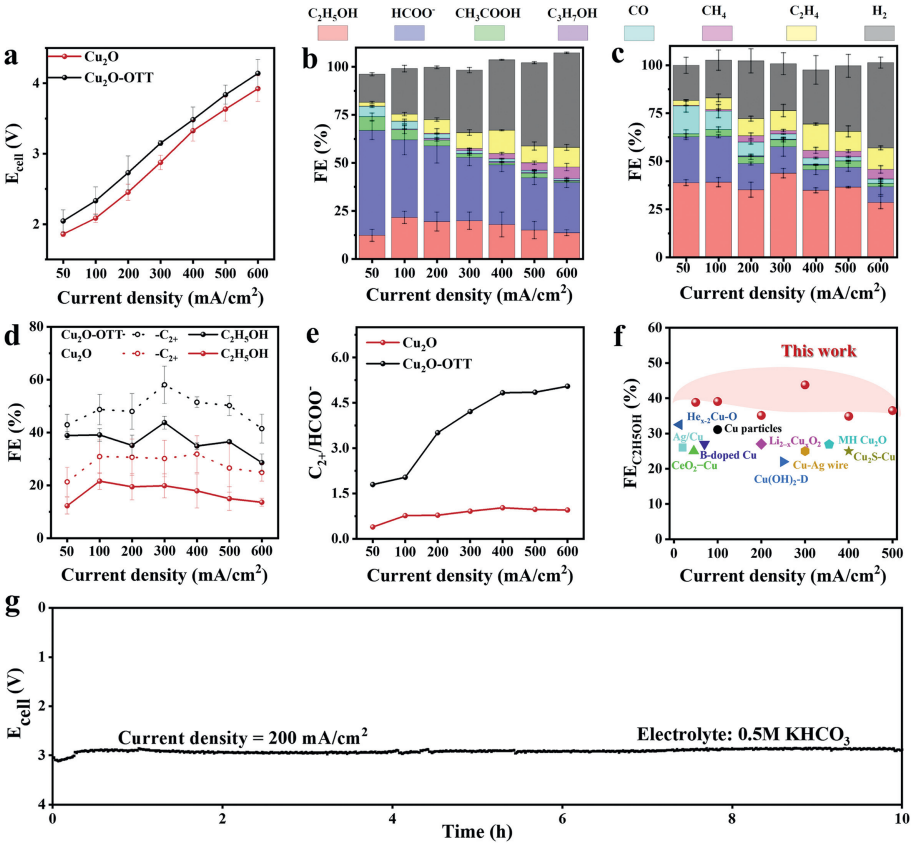



**Fig. 4.** $CO_2$RR performance in a MEA electrolyzer: (a) *I-V* curves of $Cu_2O$ and $Cu_2O$-OTT; FE of products of the (b) $Cu_2O$ and (c) $Cu_2O$-OTT. (d) FE of $C_{2+}$ and $C_2H_5OH$. (e) Ratios of $C_{2+}$ to-HCOO- for $Cu_2O$ and $Cu_2O$-OTT. (f) Performance comparison of Cu-based catalysts for $C_2H_5OH$ production by $CO_2$RR pathway. (g) Stability test of $Cu_2O$-OTT in 0.5 mol/L $KHCO_3$ electrolyte.

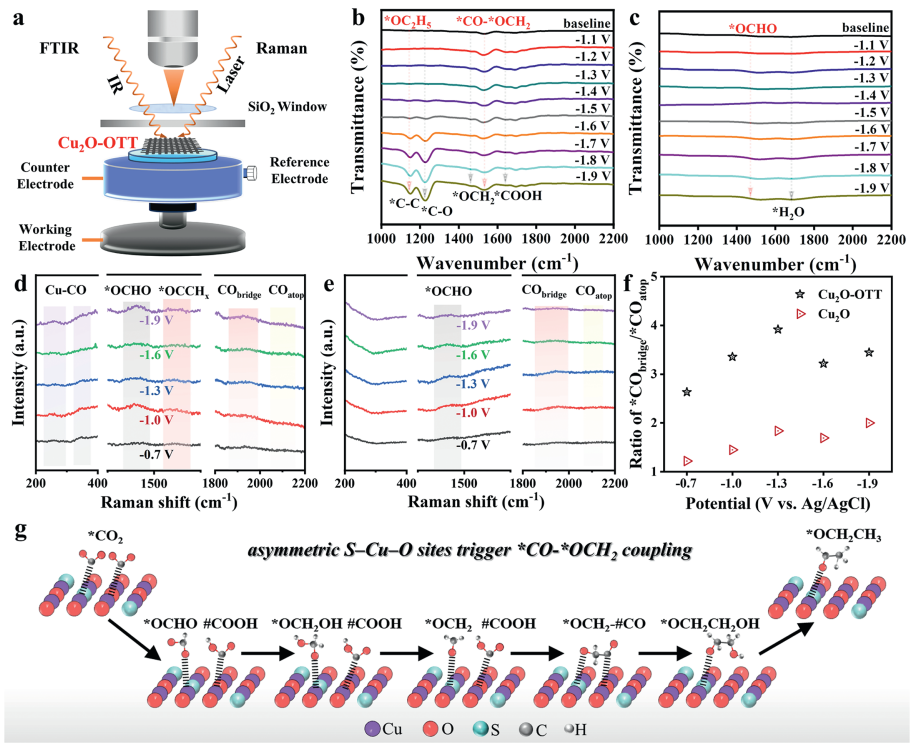



**Fig. 5.** Mechanistic investigation: (a) The schematic illustration of *in-situ* FTIR and Raman electrolytic cell. (b, c) *In-situ* FTIR spectra at different potentials *vs.* Ag/AgCl. (d, e) *In-situ* Raman spectra at different potentials *vs.* Ag/AgCl. (f) The ratio of $^*CO_{bridge}$ to $^*CO_{atop}$ obtained from Raman spectra. (g) Schematic illustration for the catalytic mechanism for $CO_2$RR to $C_2H_5OH$ on $Cu_2O$-OTT.

$cm^{-1}$ corresponding to *OCHO emerged in the Raman spectra of $Cu_2O$ (Fig. 5e).

Additionally, there appear two peaks at 1923 and 2044 $cm^{-1}$ for $Cu_2O$ and $Cu_2O$-OTT, associating with the bridge–adsorbed *CO ($*CO_{bridge}$) and atop–adsorbed *CO ($*CO_{atop}$), respectively. In general, $*CO_{bridge}$ protonation to $*OCH_2$ is proved to be more energetically favorable than that of $*CO_{atop}$ [34–36], and the ratio $*CO_{bridge}/*CO_{atop}$ for $Cu_2O$@OTT is significantly greater than that for $Cu_2O$ over the potential range (Fig. 5f), which could be in favor of $C_2H_5OH$ generated from $CO_2$ (Fig. S16 in Supporting information).

Based on the above results, we proposed a comprehensive reaction mechanism, as outlined in Fig. 5g. The $Cu_2O$ primarily follows the pathway of $CO_2$-to-HCOOH to generate $HCOO^-$ due to its inherent crystal characteristics (Fig. S15 in Supporting information). OTT layer not only creates a favorable microenvironment for $CO_2$/CO enrichment, but also allow the formation of S–Cu–O asymmetric site in $Cu_2O$-OTT electrode, which induces more *CO absorbed on the catalyst surface. Afterward, the coupling of *CO and *OCHO intermediates *via* asymmetric active sites of Cu–S and Cu–O enables significant enhancement of $C_2H_5OH$ selectivity through synergistic dual-sites pathway. Additionally, the OTT layer enriches CO, allowing C–C coupling between different adsorbed CO states to produce $C_2H_5OH$. These combined mechanisms achieve the switch of products from $HCOO^-$ to $C_2H_5OH$, and surface modification engineering strategy provides a novel perspective for designing efficient $CO_2$RR electrocatalysts.

In summary, this work demonstrates the rational design of an alkanethiol-modified $Cu_2O$ nanowire array electrocatalyst featuring asymmetric Cu–O/Cu–S dual sites for significantly enhancing $CO_2$-to-$C_2H_5OH$ conversion. The catalyst exhibits a notable $C_2H_5OH$ Faradaic efficiency of 45% at 300 $mA/cm^2$, representing a more than two-fold improvement over bare $Cu_2O$. Mechanistic studies reveal that the O–Cu–S site facilitates critical carbon-bonding interactions that stabilize key *CO and $*OCH_2$ intermediates, complementing the oxygen-affinitive nature of the Cu–O site. This asymmetric configuration enables thermodynamically favored C–C coupling between *CO and $*OCH_2$ *via* the asymmetric S–Cu–O motif, leading to the formation of the CO–$OCH_2$ intermediate and selectively promoting $C_2H_5OH$ production, in contrast to symmetric O–Cu–O sites that favor HCOOH formation. Our findings provide both a promising catalyst design strategy for multi-site synergistic $CO_2$RR and fundamental insights into the mechanism of asymmetric C–C coupling toward $C_2H_5OH$.

## Declaration of competing interest

The authors declare that they have no known competing financial interests or personal relationships that could have appeared to influence the work reported in this paper.

## CRediT authorship contribution statement

**Min Zhang:** Writing – review & editing, Writing – original draft, Visualization, Investigation, Funding acquisition, Formal analysis, Data curation, Conceptualization. **Weimin Wang:** Visualization, Data curation. **Jun Li:** Supervision, Resources. **Xun Zhu:** Supervision, Resources, Funding acquisition. **Qian Fu:** Writing – review & editing, Supervision, Resources, Funding acquisition.

## Acknowledgments

The authors are grateful for the financial supports of the National Natural Science Foundation of China (NSFC, Nos. 52394202, 52476056, and 52301232) and the Natural Science Foundation of Chongqing Province (No. 2024NSCQ-MSX1109).

## Supplementary materials

Supplementary material associated with this article can be found, in the online version, at doi:10.1016/j.cclet.2025.111926.

## References

[1] M. Zhang, A. Cao, Y. Xiang, et al., Nano-Micro Lett. 16 (2024) 50.
[2] M. Zhang, W. Wei, S. Zhou, et al., Energy Environ. Sci. 14 (2021) 4998–5008.
[3] M. Zhang, X. Wang, J. Ding, et al., Nanoscale 16 (2024) 7076–7084.
[4] M. Zhang, S. Zhou, W. Wei, et al., Chem. Catal. 2 (2022) 3528–3545.
[5] M. Zhang, Z. Tan, M. Xing, et al., J. Energy Chem. 112 (2026) 90–96.
[6] X. Wang, Z. Wang, F.P. García de Arquer, et al., Nat. Energy 5 (2020) 478–486.
[7] Z.H. Zhao, J.R. Huang, P.Q. Liao, et al., J. Am. Chem. Soc. 145 (2023) 26783–26790.
[8] J. Bi, P. Li, J. Liu, et al., Nat. Commun. 14 (2023) 2823.
[9] Z. Chen, Z. Ma, G. Fan, et al., ACS Appl. Mater. Interfaces 16 (2024) 35143–35154.
[10] G. Feng, S. Wang, S. Li, et al., Angew. Chem. Inter. Ed. 62 (2023) e202218664.
[11] A. Herzog, M.L. Luna, H.S. Jeon, et al., Nat. Commun. 15 (2024) 3986.
[12] Y. Lin, T. Wang, L. Zhang, et al., Nat. Commun. 14 (2023) 3575.
[13] P. Luan, X. Dong, L. Liu, et al., ACS Catal. 14 (2024) 8776–8785.
[14] C. Peng, J. Ma, G. Luo, et al., Angew. Chem. Int. Ed. 63 (2024) e202316907.
[15] D. Wakerley, S. Lamaison, F. Ozanam, et al., Nat. Mater. 18 (2019) 1222–1227.
[16] J. Wang, H. Yang, Q. Liu, et al., ACS Energy Lett. 6 (2021) 437–444.
[17] P. Wang, H. Yang, C. Tang, et al., Nat. Commun. 13 (2022) 3754.
[18] X. Wang, Z. Jiang, P. Wang, et al., Angew. Chem. Int. Ed. 62 (2023) e202313646.
[19] A. Xu, S.F. Hung, A. Cao, et al., Nat. Catal. 5 (2022) 1081–1088.
[20] F. Xu, B. Feng, Z. Shen, et al., J. Am. Chem. Soc. 146 (2024) 9365–9374.
[21] H. Zhang, Y. Sun, J. Wang, et al., ACS Appl. Energy Mater. 6 (2023) 11448–11457.
[22] T. Zhang, S. Xu, D.L. Chen, et al., Angew. Chem. Int. Ed. 63 (2024) e202407748.
[23] Y. Zhang, Y. Chen, X. Wang, et al., Nat. Commun. 15 (2024) 5172.
[24] J. Zhou, Q. Liang, P. Huang, et al., Nanoscale 16 (2024) 13011–13018.
[25] J. Li, R. Cai, H. Mu, et al., ACS Catal. 14 (2024) 3266–3277.
[26] X. Ma, Y. Zhang, T. Fan, et al., Adv. Funct. Mater. 33 (2023) 2213145.
[27] D. Tan, B. Wulan, J. Ma, et al., Nano Lett. 22 (2022) 6298–6305.
[28] S. Li, H. Duan, J. Yu, et al., ACS Catal. 12 (2022) 9074–9082.
[29] D. Wakerley, S. Lamaison, J. Wicks, et al., Nat. Energy 7 (2022) 130–143.
[30] X. Kong, J. Zhao, J. Ke, et al., Nano Lett. 22 (2022) 3801–3808.
[31] Y.C. Li, Z. Wang, T. Yuan, et al., J. Am. Chem. Soc. 141 (2019) 8584–8591.
[32] H. Li, P. Wei, D. Gao, et al., Curr. Opin. Green Sustain. Chem. 34 (2022) 100589.
[33] F. Li, Z. Men, S. Li, et al., Spectrochim. Acta A 189 (2018) 621–624.
[34] S. Jiang, K. Klingan, C. Pasquini, et al., J. Chem. Phys. 150 (2019) 041718.
[35] H.H. Heenen, H. Shin, G. Kastlunger, et al., Energy Environ. Sci. 15 (2022) 3978–3990.
[36] D. Karapinar, C.E. Creissen, J.G. Rivera de la Cruz, et al., ACS Energy Lett. 6 (2021) 694–706.